BPA-Based InSAR for High-Resolution DEM Generation Using UAV and Airborne Platforms

Sangho An [1], Duk-jin Kim[1*], Junwoo Kim[2]

[1]School of Earth and Environmental Science, Seoul National University, Seoul, Republic of Korea

[2]Future Innovative Institute, Seoul National University, Siheung, Republic of Korea

* djkim@snu.ac.kr

***Abstract*:** *This study investigates the application of the BPA-InSAR using both airborne and UAV platforms. The purpose of the research is to evaluate whether BPA can provide accurate and reliable DEMs under different operational conditions, ranging from stable airborne flights to lightweight UAV operations. The airborne experiment was conducted over volcanic terrain on Jeju Island with an X-band interferometric SAR system, where motion compensation based on GPS, IMU, and lever-arm corrections was applied. Results demonstrated sub-meter DEM accuracy, with improved phase stability after motion correction. UAV experiments were carried out over flat terrain with multiple corner reflectors and an independent optical UAV DEM for validation. Without motion compensation, UAV interferograms showed unstable fringe patterns and significant elevation bias. After compensation and bias correction using corner reflectors, UAV DEMs achieved sub-meter relative accuracy with RMSE values of 0.2–0.6 m compared to ground surveys and optical DEMs. These findings confirm that BPA-InSAR, when combined with proper motion compensation and minimal ground control, is effective for both airborne and UAV-based DEM generation. The study highlights BPA's versatility, demonstrating its potential for precision mapping in stable airborne campaigns as well as rapid and flexible UAV-based surveys, with implications for disaster response, environmental monitoring, and localized terrain mapping.*

Keywords: Backprojection Algorithm, InSAR, UAV SAR, Airborne SAR, Motion Compensation

Introduction

Synthetic Aperture Radar Interferometry (InSAR) has emerged as a core remote sensing technology for generating Digital Elevation Models (DEMs) and monitoring surface deformation. By exploiting the phase difference between two radar acquisitions, InSAR allows accurate reconstruction of terrain height regardless of day–night cycles or weather conditions. Over the past decades, airborne and spaceborne InSAR systems have proven their effectiveness in various applications such as topographic mapping, geohazard monitoring, infrastructure management, and natural resource exploration. Despite these achievements, challenges remain when InSAR is applied to small-scale or rapid-response scenarios, where a balance must be achieved among spatial resolution, accuracy, and operational flexibility. While airborne SAR systems have been widely used for high-resolution DEM generation, UAV-based SAR introduces unique challenges such as shorter baselines and stronger motion instabilities, which require further investigation.

At the heart of InSAR processing lies the choice of image formation algorithm. Traditionally, frequency-domain algorithms such as the Range-Doppler Algorithm (RDA) and Chirp Scaling Algorithm (CSA) have been widely used due to their computational efficiency, making them suitable for large-scale satellite data processing. However, when the flight trajectory is nonlinear or sampling irregularities occur—as is often the case with airborne or UAV platforms—frequency-domain approaches require complex corrections. In contrast, the Backprojection Algorithm (BPA) reconstructs radar images in the time domain by directly modeling the geometric distance between the antenna and each image pixel (Duersch, 2013; Cruz et al., 2022). This approach naturally accommodates nonlinear trajectories and irregular sampling, while simultaneously offering automatic coregistration between channels and implicit removal of the flat-earth phase (Lin et al., 2018; Desai etal., 2018). These unique features make BPA particularly advantageous for airborne and UAV-based operations, where precise antenna positioning and robust motion compensation are critical.

Airborne experiments provide an important environment for evaluating BPA-InSAR performance and validating the effectiveness of motion compensation techniques. Compared to UAVs, airborne platforms allow more stable operations and typically achieve higher signal-to-noise ratios (SNR), offering cleaner data for algorithm testing. Consequently, airborne data serve as a reference case to evaluate the baseline performance of BPA-InSAR under controlled conditions. In this study, we specifically investigate how the integration of GPS, IMU, and lever-arm corrections affects phase stability and DEM accuracy. By comparing interferometric results obtained with and without motion compensation, we quantitatively demonstrate the degree to which trajectory correction improves InSAR outcomes. This comparative analysis highlights one of the key strengths of BPA-InSAR in airborne environments.

On the other hand, UAV-based SAR systems bring a different set of opportunities and challenges. UAVs enable low-cost, flexible, and on-demand acquisitions, making them particularly attractive for localized mapping and rapid disaster response. However, UAV platforms face severe limitations in payload capacity, flight endurance, and motion stability (Ruiz-Carregal et al., 2024). These constraints shorten the achievable baseline, reducing height sensitivity, while simultaneously amplifying motion-induced phase errors. As a result, it is essential to validate BPA-InSAR under UAV conditions to assess whether the algorithm's advantages can translate into practical accuracy levels for lightweight platforms.

In this study, UAV experiments were conducted primarily over flat terrain to evaluate the practical feasibility of BPA-InSAR DEM generation. The UAV-based DEMs were validated against two independent references: surveyed corner reflectors (CRs) with sub-centimeter accuracy, and an optical DEM generated via structure-from-motion (SfM) photogrammetry. These cross-comparisons allow us to rigorously test whether UAV BPA-InSAR can achieve accuracy sufficient for real-world applications, even under the inherent limitations of UAV flight dynamics. The emphasis here is not only on reporting numerical accuracy but also on demonstrating operational reliability and cross-validation with independent datasets.

The contributions of this study can be summarized as follows. First, the airborne experiments systematically evaluate the impact of precise trajectory correction by comparing phase stability and DEM accuracy before and after GPS/IMU/lever-arm-based motion compensation. This highlights the role of accurate antenna positioning in maintaining interferometric quality. Second, the UAV experiments validate BPA-InSAR performance under constrained conditions by directly comparing radar-derived DEMs with CR surveys and optical DEMs, thereby confirming the algorithm's feasibility in lightweight UAV scenarios. Third, the combined analysis across both airborne and UAV platforms provides a comprehensive perspective on how BPA-InSAR performs under different operational environments, from controlled airborne settings to more constrained UAV conditions.

By integrating these two complementary experimental campaigns, the study advances the understanding of BPA-InSAR applicability across platforms with distinct operational characteristics. Airborne experiments provide insights into algorithmic robustness and motion compensation effectiveness, while UAV experiments demonstrate feasibility in practical, resource-limited scenarios. Together, they establish BPA-InSAR as a versatile approach for high-resolution DEM generation, capable of supporting both precision geospatial studies and rapid local mapping tasks.

Methodology

In this study, the BPA was adopted as the image formation technique because of its robustness in handling the nonlinear flight trajectories and irregular sampling conditions commonly encountered in both airborne and UAV-based SAR operations. Conventional frequency-domain algorithms, such as the RDA or the CSA, rely on Fourier-domain processing and assume near-linear platform motion. By contrast, BPA reconstructs radar

images directly in the time domain by explicitly calculating the geometric distance between the antenna phase center and each pixel on a predefined imaging grid (Duersch, 2013; Duersch & Long, 2015). This characteristic enables BPA to accommodate arbitrary trajectories without additional resampling or secondary corrections, making it suitable not only for UAV systems affected by gusts, sudden attitude variations, and short acquisition durations, but also for airborne campaigns conducted over complex terrain (Cao et al., 2017). The overall workflow of the proposed BPA-InSAR framework is illustrated in Figure 1.

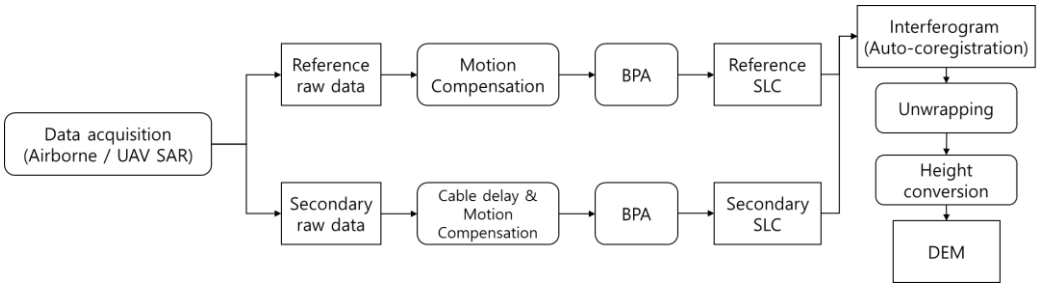

Figure 1: Workflow of the proposed BPA-InSAR processing chain

InSAR processing with BPA follows a unified workflow for both airborne and UAV datasets. Raw radar echoes acquired along the flight path are first range-compressed and then backprojected to form Single-Look Complex (SLC) images. Because all channels are reconstructed onto a common reference grid, the resulting SLC images are inherently co-registered, eliminating the need for additional spatial alignment. Moreover, BPA implicitly removes the flat-earth phase contribution, simplifying interferogram formation and subsequent DEM reconstruction.

The interferometric phase is derived by multiplying one SLC image with the complex conjugate of the other. This phase contains contributions not only from terrain but also from motion errors, baseline uncertainties, and system delays. To isolate the topographic signal, precise motion compensation is essential. In this study, GPS and IMU measurements were combined with lever-arm corrections to recover the accurate antenna trajectory. The same correction procedure was applied consistently to both airborne and UAV datasets, and the evaluation focused on how this correction improved phase stability and DEM accuracy under different operational conditions.

Finally, the corrected interferometric phase was converted into elevation through phase-to-height mapping, which accounts for radar wavelength, baseline geometry, and incidence angle. An additional refinement step was introduced after DEM generation, in which pixel

coordinates were adjusted according to the recovered heights. This post-adjustment ensured that the reconstructed DEMs were geometrically consistent with the true terrain surface. The DEMs were then validated against independent references, including surveyed CRs and an optical DEM generated via UAV-based photogrammetry.

Through this unified framework, BPA-InSAR was applied consistently to both airborne and UAV datasets using the same correction procedures and processing steps. This approach enabled a direct comparison of results across the two platforms and provided a comprehensive evaluation of BPA-InSAR performance under different operational conditions.

a. BPA Phase Modeling and Interferometric Formulation:

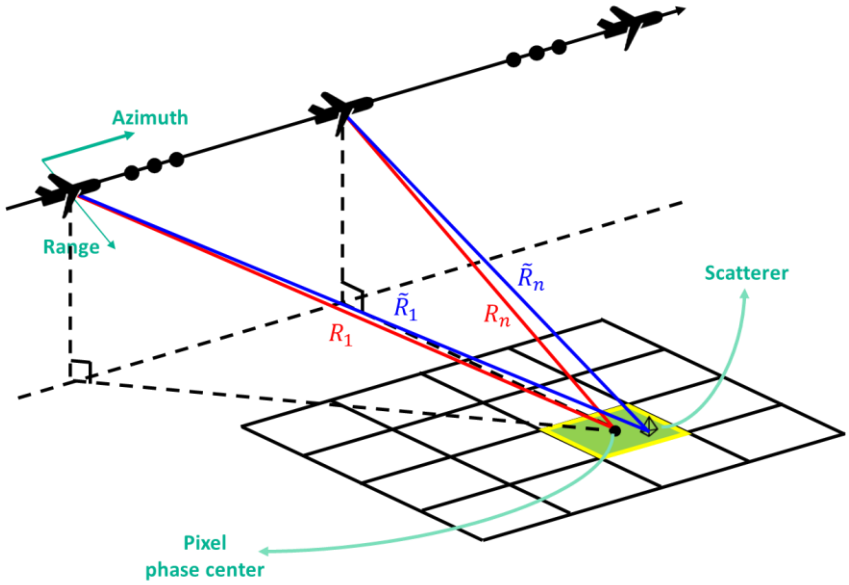

Figure 2: Geometry of the BPA

First, we analyzed the characteristics of the interferometric phase in the BPA. Specifically, we investigated how the phase values derived from BPA differ from those obtained using conventional frequency-domain InSAR processing.

When a radar pulse is transmitted from the antenna and reflected by a target, the received range-compressed signal at the antenna can be expressed as

$$s_{RC}(i) = A_i \exp(-j2\pi f_0 \tau_i) \quad (1)$$

where i is the slow-time pulse index, A_i is the signal amplitude, f_0 is the center frequency, and τ_i denotes the two-way propagation time from the antenna to the target.

For BPA processing, a reference imaging plane at a given altitude is defined, and a reconstruction grid is created with appropriate pixel spacing. The geometry of the BPA process is shown in Figure 2. The geometric distance between the antenna and the actual target is denoted as R_i, while the corresponding distance to the reference grid pixel is $\tilde{R}_i$. Using these quantities, a matched filtering operation is applied to the received signal, yielding

$$\begin{aligned} s_{RC}^{comp}(i) &= s_{RC}(i)\exp\{j2\pi f_0 \tilde{\tau}_i\} \\ &= A_i \exp\left\{-j2\pi f_0\left(\frac{2R_i}{c}-\frac{2\tilde{R}_i}{c}\right)\right\} \\ &= A_i \exp\{-jk\Delta R_i\} \end{aligned} \tag{2}$$

where $\tilde{\tau}_i = 2\tilde{R}_i/c$, $k = 4\pi/\lambda$, $\Delta R_i = R_i - \tilde{R}_i$, where λ is the radar wavelength.

The final BPA result for each pixel is obtained by coherently summing the compensated signals over the entire synthetic aperture length:

$$\begin{aligned} I_{BP} = \sum_{i=-N}^{M} s_{RC}^{comp}(i) &= \sum_{i=-N}^{M} A_i \exp\{-jk\Delta R_i\} \\ &\approx |I_{BP}| \exp\{-jk\Delta R_0\} \end{aligned} \tag{3}$$

where ΔR_0 is the range difference at the azimuth position closest to the pixel.

It should be noted that in conventional frequency-domain algorithms, the interferometric phase expression retains the absolute slant range term R. In contrast, BPA eliminates this dependency, leaving only the differential range term ΔR. This fundamental difference explains why BPA inherently performs auto-coregistration and implicit flat-earth phase removal, while frequency-domain methods require additional corrections.

b. Motion Compensation and Position Estimation:

Accurate motion compensation is essential in UAV-based BPA-InSAR because interferometric phase measurements are highly sensitive to sub-wavelength errors. Even centimeter-level position offsets or milliradian-level angular deviations can induce phase shifts comparable to, or larger than, the topographic signal of interest. While BPA can theoretically reconstruct images under arbitrary flight trajectories, the quality of the interferometric phase still depends on how precisely the antenna position is estimated at each pulse transmission.

In practice, UAVs are typically equipped with both a Global Positioning System (GPS) receiver and an Inertial Measurement Unit (IMU). The GPS provides the navigation trajectory of the platform, while the IMU records angular states—roll (ϕ_r), pitch (θ_p), and yaw (ψ_y). However, the radar antenna is rarely collocated with the GPS/IMU unit. Instead, it is mounted at a fixed offset, known as the lever arm. This offset must be corrected to determine the true antenna phase center position.

If we denote the GPS-derived position as $P_{GPS}(t)$, the lever-arm vector in the UAV body frame as I_b, and the body-to-navigation rotation matrix as $R(\phi_r, \theta_p, \psi_y)$, then the corrected antenna position is expressed as :

$$P_{ant}(t) = P_{GPS}(t) + R(\phi_r, \theta_p, \psi_y) I_b \tag{4}$$

Here, the rotation matrix $R(\phi, \theta, \psi)$ is constructed as

$$R(\phi_r, \theta_p, \psi_y) = R_z(\phi_r) R_y(\theta_p) R_x(\psi_y) \tag{5}$$

With R_z, R_y, R_x representing the rotation matrices corresponding to roll, pitch, and yaw, respectively. This formulation highlights how angular variations measured by the IMU propagate into antenna position errors. The lever-arm geometry and antenna motion due to roll, pitch, and yaw are depicted in Figure 3.

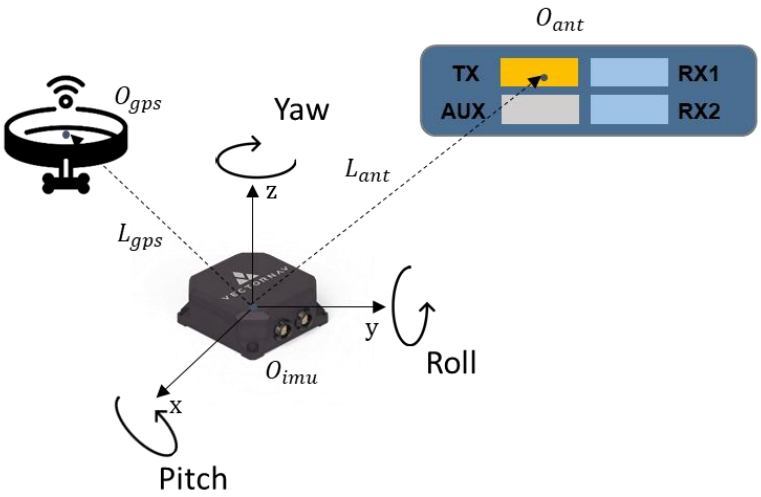

Figure 3: Antenna motion caused by roll, pitch, and yaw variations.

For example, when the lever arm has a vertical offset l_z, a small roll error $\Delta\phi$ results in a lateral displacement of approximately $l_z \cdot \Delta\phi$. Similarly, pitch errors cause forward–backward displacement, and yaw errors lead to horizontal shifts relative to the flight direction. In UAV configurations where the antenna is mounted tens of centimeters away from the navigation sensors, even small angular deviations can lead to centimeter-scale errors in antenna position, corresponding to significant interferometric phase biases.

The impact of such residual errors on the measured phase can be written as

$$\Delta\varphi(t) = \frac{4\pi}{\lambda}\hat{r}(t) \cdot \Delta r(t) \tag{6}$$

where $\hat{r}(t)$ is the unit vector pointing from the antenna to the target, and $\Delta r(t)$ denotes the antenna position error due to imperfect compensation. This expression shows that both translational inaccuracies in GPS-derived positions and rotational deviations from roll, pitch, and yaw directly contribute to phase noise.

In this study, motion compensation was implemented by combining GPS and IMU data. The GPS provided the global navigation trajectory, while the IMU measurements were used to rotate the lever-arm vector, yielding corrected antenna phase center positions. These corrected positions were then applied during the BPA matched filtering step, ensuring that the reconstructed SLC images were referenced to the most accurate antenna trajectory available. By applying motion compensation at the image formation stage rather than after interferogram generation, residual motion-induced phase distortions were effectively reduced, leading to more reliable interferometric measurements and improved DEM accuracy (Cao et al., 2017; Xie et al., 2019).

c. Phase-to-Height Conversion for DEM Generation:

The final objective of interferometric processing is to convert the measured phase differences into terrain elevation (Xu et al., 2020; Duersch, 2013). For a given pixel, the interferometric phase ϕ is proportional to the path length difference between the two radar channels, which in turn is related to the elevation of the target relative to the reference imaging plane. This relationship can be expressed as

$$h = -\frac{\lambda R_0 \phi \sin\theta_0}{4\pi B_\perp \cos(\theta_0 - \xi)} \tag{7}$$

where h denotes the target height relative to the reference plane, θ_0 is the incidence angle at the reference grids, $B_\perp$ is the perpendicular component and ξ is the tilt angle of the baseline between the two channels, and R_0 is the slant range distance from the antenna to the target. In practice, the proportionality between phase and height depends strongly on both the baseline geometry and the local incidence angle θ_0, meaning that DEM sensitivity varies across the scene.

In UAV-based BPA-InSAR, phase-to-height mapping requires particular care because UAV trajectories typically result in relatively short baselines compared to airborne or spaceborne platforms. Short baselines are advantageous in preserving interferometric coherence, but they also reduce the sensitivity of the interferometric phase to terrain height, thereby lowering the vertical resolution of the DEM. Conversely, longer baselines increase sensitivity to elevation but may also introduce geometric decorrelation. Thus, the baseline must be selected to balance sensitivity and coherence—a trade-off that is especially critical in UAV campaigns where flight paths are constrained by endurance, safety, and operational limitations.

Another key factor is the incidence angle. Pixels imaged at shallow incidence angles (closer to nadir) exhibit reduced sensitivity to height, while those imaged at steeper angles (closer to grazing) provide greater height sensitivity but are more susceptible to layover and shadowing effects. In this study, flights were designed to include two different incidence angles, enabling an evaluation of how imaging geometry affects DEM accuracy and stability.

It should also be noted that BPA reconstructs pixels on a predefined reference plane. As a result, when the actual terrain height deviates from this reference plane, the horizontal location of each pixel may not perfectly correspond to its true ground position after DEM generation. To address this issue, an additional correction step was applied, in which pixel coordinates were adjusted based on the final elevation values. This post-adjustment ensures that the reconstructed DEM is geometrically consistent with the actual terrain surface.

After phase unwrapping, phase-to-height conversion, and post-adjustment of pixel coordinates, the reconstructed DEM can be georeferenced and validated against independent references. In this study, the generated DEMs were compared with surveyed CR elevations and an optical UAV-derived DEM. This multi-source evaluation confirms that the proposed phase-to-height conversion is not only theoretically sound but also practically accurate under UAV operating conditions.

d. Experimental Setup:

To validate the proposed BPA-InSAR framework, two complementary experimental campaigns were carried out: one using an airborne SAR system and the other employing a UAV-based SAR system. Although the two platforms operated under very different conditions, both datasets were processed using the same backprojection-based interferometric workflow to enable consistent evaluation and comparison.

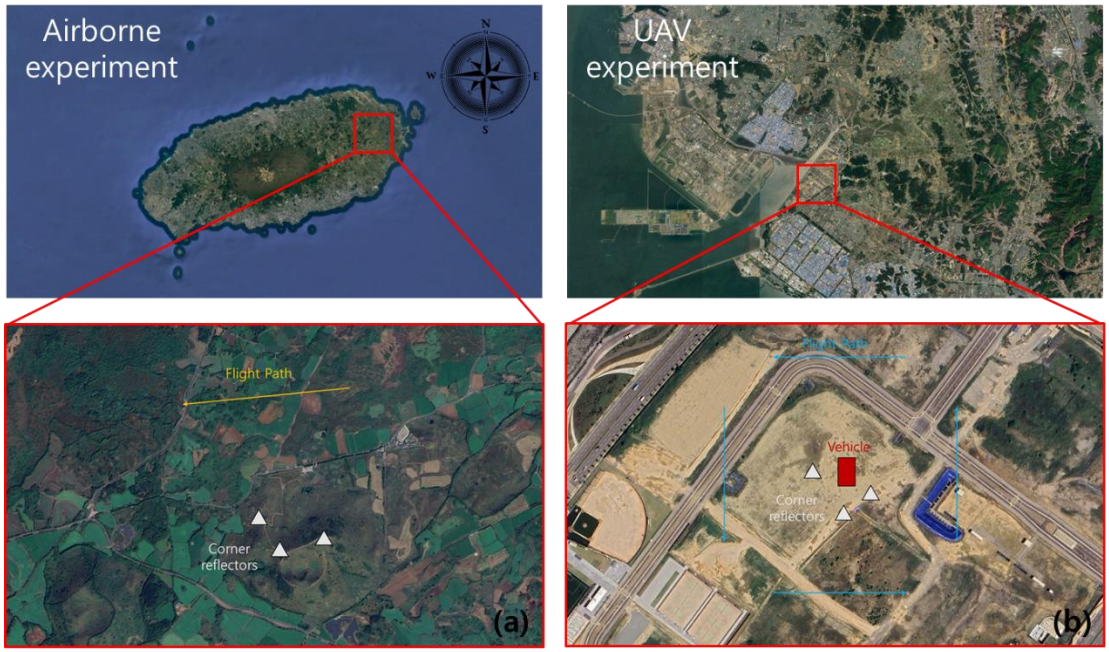

Figure 4: Experimental sites: (a) Jeju airborne campaign, (b) Siheung UAV campaign

The locations of the airborne and UAV experiments are shown in Figure 4. The airborne experiment was conducted over the Yongnuni Oreum volcanic terrain on Jeju Island using an X-band interferometric SAR system operated in stripmap mode. The aircraft flew at an altitude of approximately 630 m along a flight distance of about 830 m, with a central incidence angle of 42°. The perpendicular baseline between the two receiving channels was about 0.18 m, and the radar wavelength was 0.0292 m. The system was designed to achieve high-resolution DEM generation, with the reconstructed imagery providing a spatial resolution better than 1 m. Precise antenna trajectories were estimated by integrating GPS and IMU measurements with lever-arm corrections. CRs were deployed on the ground to serve as reference points for interferometric phase calibration, and the reconstructed DEM was validated against independent ground survey data.

The UAV experiment was conducted over a flat-terrain site to evaluate the feasibility of BPA-InSAR under lightweight platform conditions. A compact X-band SAR system was mounted on the UAV and operated in stripmap mode. The flights were carried out at a fixed incidence angle from four different azimuthal directions, with multiple CRs and a vehicle deployed as reference targets. The UAV flew at an altitude of approximately 90 m over a flight distance of 160 m, with a central incidence angle of about 60°. The perpendicular baseline was about 0.1 m, and the radar wavelength was the same as in the airborne experiment, 0.0292 m. The short baselines provided stable coherence but limited vertical sensitivity. To provide an independent validation, an optical UAV was simultaneously deployed to acquire overlapping images of the same site. These images were processed using a SfM pipeline to generate an optical DEM (Westoby et al., 2012; Smith et al., 2016). The CRs were surveyed with ground-based equipment at centimeter-level accuracy, enabling precise point-based validation of the BPA-InSAR DEM, while the optical DEM provided an area-based reference for cross-validation (Žabota & Kobal, 2021; Over et al., 2021).

Together, the airborne and UAV experiments represented complementary scenarios: the airborne campaign provided a stable, higher-altitude environment, while the UAV campaign captured the constraints of a low-altitude, lightweight platform. Applying the same BPA-InSAR workflow to both datasets enabled a comprehensive assessment of performance across different operational conditions. A summary of the key experimental parameters for the airborne and UAV campaigns is provided in Table 1.

Table 1: Summary of Experimental Parameters

Parameter	Airborne SAR	UAV SAR
Platform Altitude	630 m	90 m
Flight Distance	830 m	160 m
Center Incidence	42 °	60 °
Baseline Length	0.18 m	0.1 m
Wavelength	0.0292 m	0.0292 m
Resolution	0.3 m	0.3 m

Results and Discussion

This study evaluated the performance of the BPA-InSAR framework using data acquired from two platforms: an airborne SAR system over complex volcanic terrain and a UAV-based SAR system over flat ground with controlled reference targets. The airborne experiment was designed to test the method under large-scale, relatively stable conditions, while the UAV

experiment provided insight into low-altitude operations where short baselines and platform instabilities strongly affect interferometric phase recovery. In both cases, interferograms before and after motion compensation were compared, enabling a clear assessment of how trajectory corrections influence phase stability and DEM accuracy.

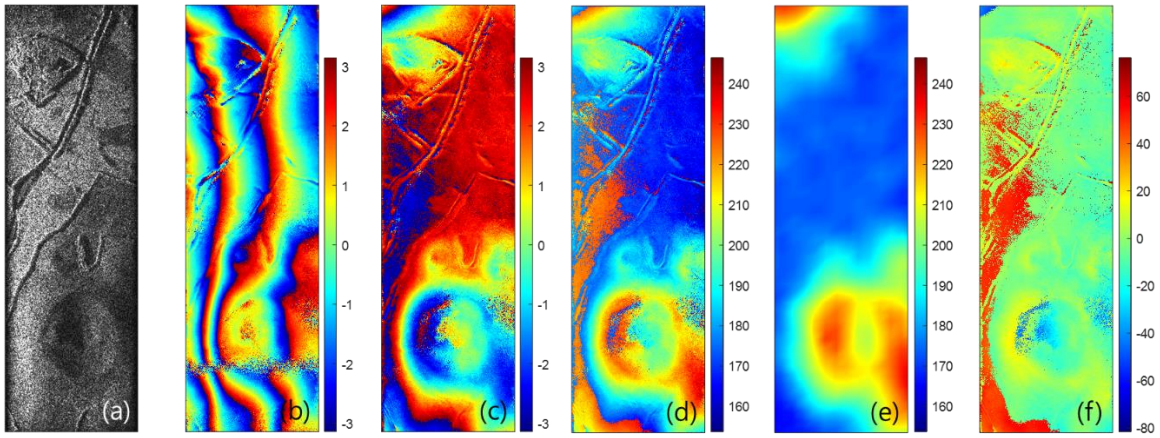

Figure 5: Airborne BPA-InSAR results: (a) amplitude, (b) interferogram before motion compensation, (c) interferogram after motion compensation, (d) DEM from BPA-InSAR, (e) reference SRTM DEM, (f) difference between airborne DEM and SRTM.

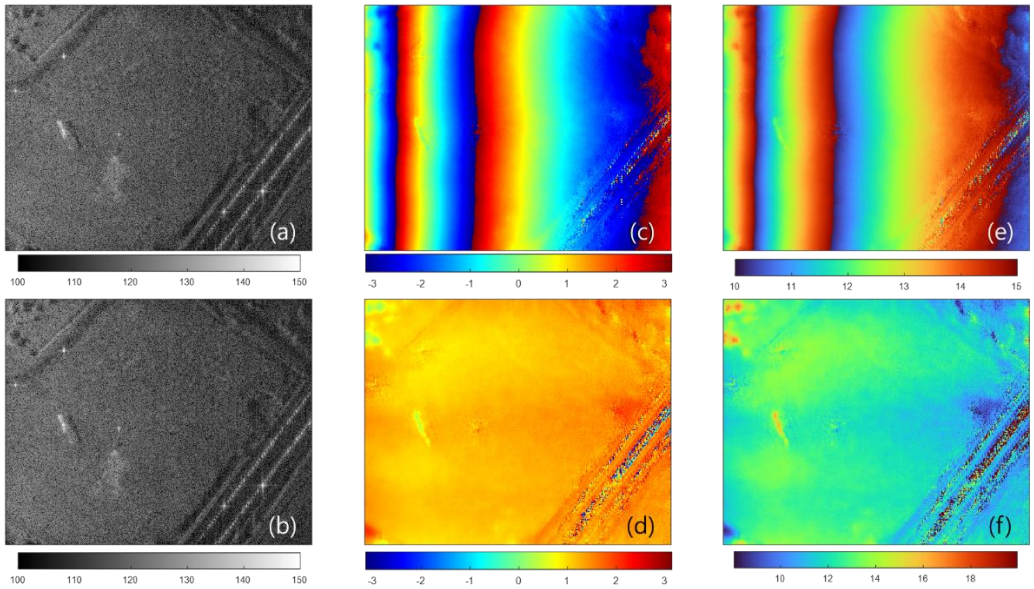

Figure 6: UAV BPA-InSAR results: Top row – before motion compensation; Bottom row – after motion compensation. From left to right: amplitude, interferogram, DEM.

The airborne BPA-InSAR results are presented in Figure 5. For the airborne dataset, the BPA amplitude images exhibited good focusing performance across the scene. CRs appeared as

strong point scatterers, while ridges and slopes were preserved as distributed scatterers. Without motion compensation, the interferometric phases showed irregular fringe patterns, and unstable phase behavior was visible around CRs. After compensation, fringe structures became more stable and better aligned with the underlying terrain. While coherence values did not increase significantly, the stabilization of fringes improved phase consistency and enabled reliable DEM generation. The reconstructed DEM achieved sub-meter agreement with a reference DEM, demonstrating that airborne BPA-InSAR can provide high-accuracy terrain measurements under complex topographic conditions.

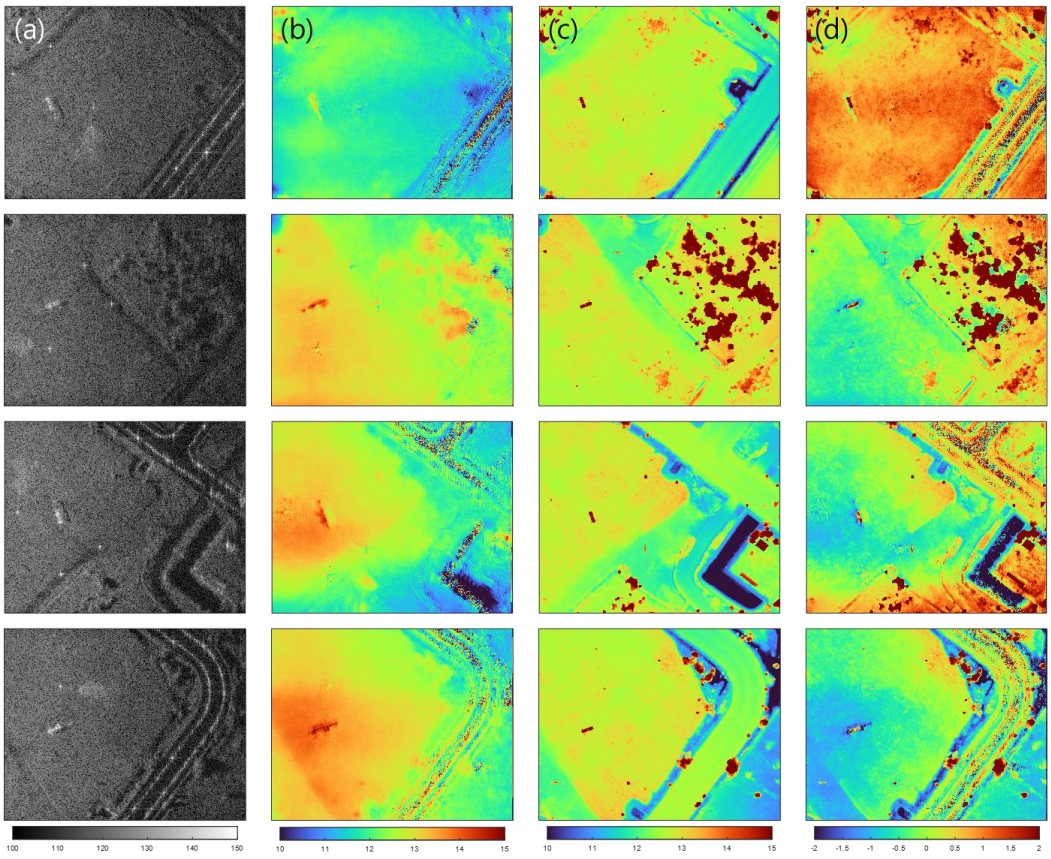

Figure 7: UAV multi-pass results: (a) amplitude, (b) UAV DEM, (c) optical DEM, (d) DEM difference.

The UAV experiment was conducted over flat terrain, with four stripmap flights flown from different azimuth directions. Three CRs and a vehicle were deployed in the scene to provide controlled reference targets. The BPA amplitude images showed the CRs clearly as point scatterers and preserved the distributed reflections from the vehicle. However, without motion compensation, the interferograms exhibited very poor coherence, with unstable phases even

around the CRs, making DEM generation impossible. This result reflects the susceptibility of UAV platforms to centimeter-level trajectory errors and milliradian-scale roll and pitch variations, which directly translate into interferometric phase noise.

After applying motion compensation using GPS/IMU trajectory data and lever-arm corrections, the interferograms improved significantly. The UAV results before and after motion compensation are illustrated in Figure 6. Fringe patterns stabilized, CR phases became coherent, and DEM reconstruction was feasible (Cao et al., 2017; Xie et al., 2019). Quantitative evaluation was then performed using surveyed CR elevations and an optical UAV DEM generated via SfM photogrammetry (Westoby et al., 2012; Žabota & Kobal, 2021). At the CR locations, the uncompensated DEMs showed a consistent positive bias of about +1.5 m, with RMSE values around 1.6 m. After applying a simple constant bias correction using the CRs as reference points, the RMSE dropped to 0.2–0.6 m, indicating that UAV BPA-InSAR can achieve sub-meter relative accuracy once systematic errors are removed. The elevation differences at the three CR locations are summarized in Table 2, confirming the presence of a systematic positive bias in the UAV DEM prior to correction.

Table 2: CR Elevation Validation (UAV SAR).

CR ID	GPS Elevation (m)	SAR DEM Elevation (m)	Difference (m)
Platform Altitude	11.225	12.355	+1.13
Flight Distance	11.250	12.672	+1.42
Center Incidence	11.773	11.891	+0.12
Mean	-	-	+0.89
RMSE	-	-	1.02

Comparison with the optical UAV DEM also confirmed these findings. A comparison of UAV DEMs, optical DEMs, and their differences is given in Figure 7. Across the four UAV flights, average differences ranged from –0.41 m to +0.83 m, with RMSE values of 0.39–0.86 m. This level of agreement is consistent with the CR-based validation and indicates that, despite UAV-specific instabilities, the reconstructed DEMs are generally reliable. Error maps showed that after bias correction, most pixels were within ±0.5 m of the optical DEM, with larger deviations confined to peripheral regions where coherence was lower. The statistical differences between UAV SAR DEMs and the optical DEM across four flight passes are presented in Table 3.

Table 3: Comparison Between UAV SAR DEM and Optical DEM.

Pass #	Mean Error (m)	RMSE (m)
Pass 1	+0.45	0.52
Pass 2	-0.12	0.39
Pass 3	+0.83	0.86
Pass 4	-0.41	0.47
Average	+0.19	0.56

The impact of motion compensation is further illustrated by visual comparisons. Interferograms without compensation displayed unstable fringes and incoherent CR signatures, while compensated interferograms exhibited stable fringe patterns and coherent CR phases. Cross-sections through CR locations also confirmed the improvement: uncompensated DEMs consistently overestimated elevations by about 1.5 m, while compensated and bias-corrected DEMs closely matched the surveyed values. These results confirm that systematic bias, rather than random noise, is the dominant error in UAV interferometry, and that it can be effectively mitigated with CR-based calibration.

Taken together, the airborne and UAV experiments confirm the robustness of the BPA-InSAR framework across different platforms. For the airborne data, motion compensation had only a modest impact on coherence values but improved fringe stability and ensured sub-meter DEM accuracy. For the UAV data, compensation was indispensable: without correction, interferograms were unusable, while with correction and CR-based bias removal, DEMs achieved sub-meter accuracy consistent with independent references. This demonstrates that BPA-InSAR can provide reliable results not only in stable airborne operations but also in challenging UAV scenarios where platform instability is a major concern.

The findings provide several important implications. First, motion compensation is essential for both airborne and UAV interferometry. Even small position or attitude errors degrade phase stability and can significantly reduce DEM accuracy, underscoring the importance of integrating GPS, IMU, and lever-arm corrections. Second, UAV DEM errors were shown to be dominated by constant bias rather than random noise, and this bias can be effectively corrected using CRs or other ground references. This suggests a practical strategy for UAV interferometry: with minimal ground control, UAV-based BPA-InSAR can achieve accuracies sufficient for real-world applications. Third, the use of both CR surveys and optical DEMs for cross-validation highlights the value of multi-source evaluation frameworks for ensuring reliability in UAV-based DEM studies.

At the same time, the experiments revealed some limitations. UAVs inherently operate with short baselines, which favor coherence but limit the sensitivity of interferometric phase to elevation, reducing vertical resolution. UAVs are also more susceptible to sudden angular deviations th an manned platforms, and while GPS/IMU corrections mitigate many of these effects, residual phase errors remain in certain areas. The optical UAV DEMs used for validation were generated without ground control points, so their absolute accuracy is uncertain. As a result, discrepancies between SAR and optical DEMs cannot be fully attributed to SAR errors. Finally, the need for CRs to correct systematic bias introduces practical constraints, especially for large-scale surveys or remote environments.

In summary, the results show that BPA-InSAR, when combined with motion compensation and bias correction, provides a robust approach to DEM generation across both airborne and UAV platforms. The airborne experiments confirmed its reliability under complex terrain conditions, while the UAV experiments demonstrated that even with platform instabilities and short baselines, sub-meter DEM accuracy can be achieved. By integrating SAR interferometry with ground-based CR surveys and optical photogrammetry, the study also established a framework for rigorous multi-source validation. These outcomes indicate that UAV BPA-InSAR is a practical and effective tool for rapid, local-scale DEM generation and has strong potential for applications in disaster response, environmental monitoring, and terrain mapping where flexible and lightweight radar platforms are advantageous.

Conclusion and Recommendation

This study evaluated the BPA-InSAR using airborne and UAV datasets. Both experiments applied the same processing chain, allowing direct comparison across platforms.

The airborne experiment demonstrated that BPA-InSAR can achieve sub-meter DEM accuracy under complex terrain conditions. Motion compensation improved fringe stability, even though coherence gains were modest, and enabled reliable phase recovery for accurate DEM reconstruction.

The UAV experiment, conducted over flat terrain with corner reflectors and a vehicle, highlighted the sensitivity of interferometric phase to UAV instabilities. Without motion compensation, interferograms were incoherent and DEM generation was impossible. After GPS/IMU and lever-arm corrections, stable fringes and coherent CR signatures were obtained. DEM validation showed a systematic positive bias of about 1.5 m, which, once corrected using CRs, reduced RMSE to the 0.2–0.6 m range. Comparisons with optical

UAV DEMs confirmed the consistency of the corrected results, though localized discrepancies remained in low-coherence regions.

These results demonstrate that motion compensation is critical for both airborne and UAV interferometry, and that UAV DEM errors are dominated by systematic biases rather than random noise (Cao et al., 2017; Xie et al., 2019). While UAV payload and short baseline constraints limit vertical sensitivity, bias correction and cross-validation with optical and ground survey data enable sub-meter accuracy.

Future research should focus on enhancing motion compensation with more precise navigation sensors, reducing reliance on corner reflectors for bias correction, and extending UAV BPA-InSAR to time-series monitoring of surface changes. Overall, the findings confirm BPA-InSAR as a practical approach for generating high-resolution DEMs and provide a foundation for its broader use in geospatial applications.

Acknowledgement

This research was supported by Korea Institute of Marine Science & Technology Promotion(KIMST) funded by the Korea Coast Guard(RS-2023-00238652, Integrated Satellite-based Applications Development for Korea Coast Guard).

Reference

Duersch, M. I. (2013). Backprojection for synthetic aperture radar. Brigham Young University.

Cruz, H., Véstias, M., Monteiro, J., Neto, H., & Duarte, R. P. (2022). A review of synthetic-aperture radar image formation algorithms and implementations: A computational perspective. *Remote Sensing, 14(5), 1258.*

Lin, J., Lv, X., & Li, R. (2018). Automatic registered back-projection approach based on object orientation for airborne repeat-track interferometric SAR. *IET Radar, Sonar & Navigation, 12(9), 1066-1076.*

Desai, K., Joshi, P., Chirakkal, S., Putrevu, D., & Ghosh, R. (2018). Analysis of performance of flat earth phase removal methods. *The International Archives of the Photogrammetry, Remote Sensing and Spatial Information Sciences, 42, 207-209.*

Ruiz-Carregal, G., Lort Cuenca, M., Yam, L., Masalias, G., Makhoul, E., Iglesias, R., ... & Duro, J. (2024). Ku-band SAR-drone system and methodology for repeat-pass interferometry. *Remote Sensing, 16(21), 4069.*

Duersch, M. I., & Long, D. G. (2015). Backprojection SAR interferometry. *International Journal of Remote Sensing, 36(4), 979-999.*

Cao, N., Lee, H., Zaugg, E., Shrestha, R., Carter, W. E., Glennie, C., ... & Yu, H. (2017). Estimation of residual motion errors in airborne SAR interferometry based on time-domain backprojection and multisquint techniques. *IEEE Transactions on Geoscience and Remote Sensing, 56(4), 2397-2407.*

Xie, P., Zhang, M., Zhang, L., & Wang, G. (2019). Residual motion error correction with backprojection multisquint algorithm for airborne synthetic aperture radar interferometry. *Sensors, 19(10), 2342.*

Xu, B., Li, Z., Zhu, Y., Shi, J., & Feng, G. (2020). SAR interferometric baseline refinement based on flat-earth phase without a ground control point. *Remote Sensing, 12(2), 233.*

Westoby, M. J., Brasington, J., Glasser, N. F., Hambrey, M. J., & Reynolds, J. M. (2012). 'Structure-from-Motion'photogrammetry: A low-cost, effective tool for geoscience applications. *Geomorphology, 179, 300-314.*

Smith, M. W., Carrivick, J. L., & Quincey, D. J. (2016). Structure from motion photogrammetry in physical geography. *Progress in physical geography, 40(2), 247-275.*

Žabota, B., & Kobal, M. (2021). Accuracy assessment of uav-photogrammetric-derived products using PPK and GCPs in challenging terrains: In search of optimized rockfall mapping. *Remote Sensing, 13(19), 3812.*

Over, J. S. R., Ritchie, A. C., Kranenburg, C. J., Brown, J. A., Buscombe, D. D., Noble, T., ... & Wernette, P. A. (2021). Processing coastal imagery with Agisoft Metashape Professional Edition, version 1.6—Structure from motion workflow documentation *(No. 2021-1039). US Geological Survey.*